ETHZ-IPP Internal Report 2009-04
February 2009

Study of the Cross-Section Measurement of the B^+ Production at the CMS Experiment

Master Thesis

presented by Katarina Gromova

under the supervision of
Prof. Dr. Urs Langenegger

ETH Zürich, Switzerland

Abstract

This thesis presents a study of the measurement of the differential cross-section of B^+ production at the CMS experiment. The cross-section is calculated using the reconstructed $B^+ \to J/\psi(\to \mu^+\mu^-)K^+$ decay channel, where the signal events are extracted by fitting the B mass-peak. The B production cross-section is measured as a function of $p_T(B)$ and compared with the generated cross-section. In this analysis, a data sample corresponding to an integrated luminosity of only $0.708\,\mathrm{pb}^{-1}$ is used. Thus, this method of determination of the differential cross-section can be used in the startup phase of the LHC.

Contents

1 Introduction **3**
- 1.1 Motivation . . . 3
- 1.2 Heavy Flavor Production . . . 3
- 1.3 Signal Channels . . . 4
- 1.4 The CMS Experiment . . . 5

2 Monte Carlo Samples **7**
- 2.1 Production . . . 7
- 2.2 Data Sample . . . 8
- 2.3 Signal Sample . . . 8

3 Event Reconstruction **8**
- 3.1 Signal Signature . . . 8
- 3.2 B Reconstruction . . . 9
- 3.3 Candidate Selection . . . 11
- 3.4 Fitting Signal Peaks . . . 14
  - 3.4.1 Gaussian Fitting . . . 16
  - 3.4.2 Double Gaussian Fitting . . . 17
  - 3.4.3 Resolutions of p_T and η . . . 17

4 Measurement of Differential Cross-Section **19**
- 4.1 Transverse Momentum Binning . . . 22
- 4.2 Fitting the Peaks . . . 23
- 4.3 Efficiency Determination . . . 23
  - 4.3.1 Muon Acceptance . . . 23
  - 4.3.2 Muon Identification Efficiency . . . 23
  - 4.3.3 m(J/ψ) Cut . . . 26
  - 4.3.4 Kaon Acceptance . . . 26
  - 4.3.5 Kaon Reconstruction Efficiency . . . 27
  - 4.3.6 ΔR(J/ψ K) Cut . . . 27
  - 4.3.7 B Efficiency . . . 27
  - 4.3.8 χ^2 Efficiency . . . 28
  - 4.3.9 Dimuon Efficiency . . . 28
  - 4.3.10 Verification of the Total Efficiency . . . 29
- 4.4 Cross-Section Results . . . 29

5 Conclusions **31**
- 5.1 Transverse Momentum Binning . . . 31
- 5.2 Fitting the Peaks . . . 31
- 5.3 Efficiencies and Differential Cross-Section . . . 32

A Acknowledgments **35**

1 Introduction

1.1 Motivation

The quest for yet undetected particles at the LHC presumes a precise knowledge of the background processes, specifically of their cross-sections. In contrast to the light u, d and s quarks, which can be obtained from a number of sources, the heavy b and c quarks have sufficiently big masses to make their production perturbatively calculable. Furthermore, the long lifetime of these quarks implies that b and c hadrons can be formed and observed. Their identification in the data is possible via reconstruction of secondary vertices, properties of prompt leptons and kinematical constraints. That is the reason why the b and c quarks are excellent probes of standard processes or various kinds of new physics. This thesis presents a method of measuring the differential cross-section of the B^+ production for low luminosity, which makes this method suitable for the startup phase of the LHC.

1.2 Heavy Flavor Production

Unlike the situation at an e^+e^--collider, in a hadron machine there is a great variety of initial states involved in the production of particles. At the energies available at the LHC, the constituents of the protons form a veritable soup of quarks and gluons, far beyond a simple uud valence-quark combination of the proton. Thus, there are many possibilities to combine quarks out of this soup to form new particles. In this thesis, we are interested in the production of heavy quarks and for this reason, one has to take a look at how these quarks can be produced. The various channels for the production of heavy quarks can be classified in three general categories, that are listed below:

Gluon-gluon fusion / quark-antiquark fusion These are the leading order processes, where two constituents (either two gluons or a quark-antiquark pair) of the initial protons directly produce a heavy quark-antiquark pair. The corresponding Feynman diagrams are depicted in figures 1 and 2. Characteristically the two final states, involving the heavy quarks, are observed 'back-to-back', i.e. with little to no combined transverse momentum.

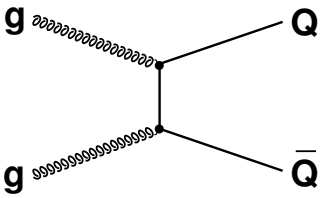

Figure 1: Gluon-gluon fusion

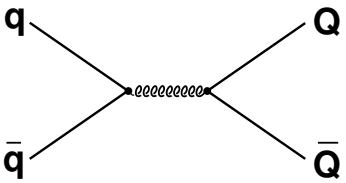

Figure 2: $q\overline{q}$ fusion

Flavor excitation Flavor excitation is a next-to-leading order processes with three interaction vertices. Here a heavy flavor quark out of a $g \to Q\overline{Q}$ process within one proton of one beam is scattered against a parton of the other beam (see fig. 3).

Gluon splitting Gluon spitting takes place when a gluon scatters off a hard gluon or quark, and splits up into a quark-antiquark pair: $g \to Q\overline{Q}$. This branching occurs in the final state of the shower (see fig. 4).

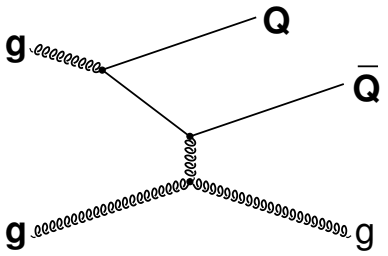

Figure 3: Flavor excitation

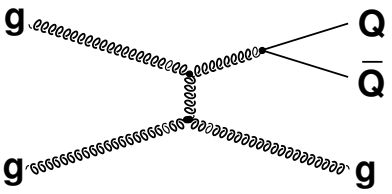

Figure 4: Gluon-splitting

Table 1: Assignment of quarks to numbers

Number	0	1	2	3	4	5
Quark	d	u	s	c	b	t

The contribution of these three kinds of heavy flavor production depends on the center-of-mass energy of the protons. For the LHC with its center-of-mass energy of 14 TeV, the main process should be flavor-excitation [1]. This also can be shown in the following figure 5. In this histogram all quarks were associated with numbers as in table 1; the three process types to numbers $0-2$:

- $0 \leftrightarrow$ Gluon-Gluon Fusion
- $1 \leftrightarrow$ Flavour Excitation
- $2 \leftrightarrow$ Gluon Splitting

Each bin of the histogram is composed out the quark and process types via the relation: bin = quark$\times$10 + process. According to this assignment, all quarks were considered on the generator level after the application of the dimuon filter, that will be explained later (see chapter 2). The process types of the quarks were filled into a histogram together with the quark number. So for example a c-quark that is produced via gluon-gluon fusion would be filled in bin 30, where "3" denotes the quark type and "0" the process type. In figure 5 one can see that most of the events corresponding to the creation of the b-quark lie in bin 41. Following the convention above it can be decoded as "4", i.e. a b-quark, and "1", i.e. flavour excitation.

In this analysis we will focus on the production of B^+, i.e. the combination of a heavy $\bar{b}$ quark with u. In order to have less statistical errors, the B^- is also used in the analysis. That means that a produced b-quark fragments into a B^+ or B^- meson and so creates a signal event that can be used to determine the differential cross-section. The probability of such a $b \to B^{\pm}$ process is roughly 40 % [2].

1.3 Signal Channels

The decay channels of $B^+ \to J/\psi(\to \mu^+\mu^-)K^+$ and $B^- \to J/\psi(\to \mu^+\mu^-)K^-$ are used for the analysis and denoted by $B \to J/\psi(\to \mu^+\mu^-)K$ in the future. Because a full reconstruction method is used in the analysis, one has to be able to identify both muons and the kaon out of the data.

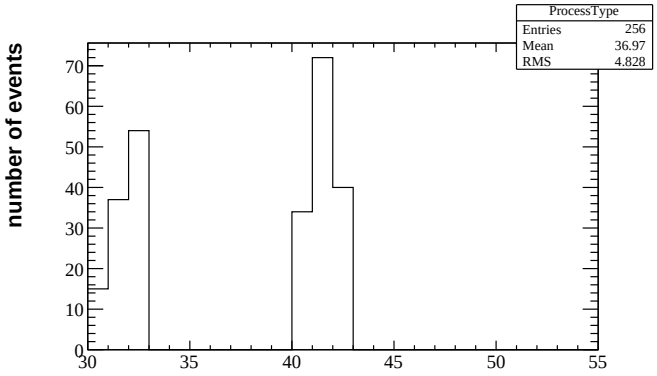

Figure 5: Distribution of production types

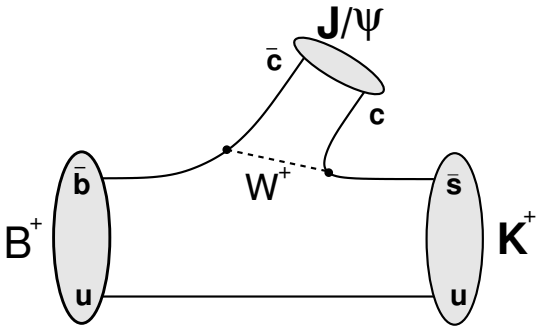

Figure 6: Feynman diagram for the process $B \to J/\psi\, K$

In the following figure 6 the decay process is shown. Due to weak interaction, the $\overline{b}$ changes into a $\overline{c}$ and the weak interaction boson W^+ produces a $c\overline{s}$ combination, leading to the formation of the J/ψ and a K. The branching fraction of this $B^+ \to J/\psi K^+$ channel is only 1.008×10^{-3}. The J/ψ particle then decays into a $\mu^+\mu^-$ pair with a branching fraction of 5.93×10^{-2}. Altogether it means that out of approximately 17000 events containing a B^+, there is one $B^+ \to J/\psi(\to \mu^+\mu^-)K^+$ decay. Besides it is clear that not every decay that took place can be reconstructed, because a muon or a kaon could miss in the data. It means that one has to accumulate an adequate amount of data to have enough reconstructed signal events and so be able to determine the differential cross-section.

1.4 The CMS Experiment

The Large Hadron Collider (LHC) is a particle accelerator located at CERN, near Geneva, Switzerland. It is the world's largest particle accelerator, working at the world's highest energies at the moment. The collider is contained in a 27 kilometer circumference tunnel at a depth of 100 meter, which was used for the Large Electron-Positron Collider (LEP) before. The collider consists of two pipes enclosed with superconducting magnets and cooled by superfluid helium, each pipe containing a proton beam. Additional magnets are placed to direct the beams to four interaction points where interactions between them take place. The protons each have an energy of 7 TeV, giving a total collision energy of 14 TeV. Beams of lead nuclei will be also accelerated, colliding at an energy of 1150 TeV. The experiments that are approved for the LHC are ATLAS, CMS, ALICE,

LHCb and TOTEM.

The Compact Muon Solenoid (CMS) experiment is one of two large general-purpose particle physics detectors built on the LHC. The complete detector is cylindrical, 21 meters long, 15 meters in diameter and approximately 12500 tons (see fig. 7). The main goals of the experiment are to explore physics at the TeV scale, so to discover the Higgs boson, to look for evidence of physics beyond the standard model (such as supersymmetry or extra dimensions) and to be able to study aspects of heavy ion collisions. There is a great experimental challenge arising due to the design luminosity leading to an event rate of approximately 10^9 pp interactions per second. This implies around 1000 charged particles emerging from the interaction region every 25 ns. For this reason the products of an interaction may be confused with particles from other interactions in the same bunch crossing. This effect can be reduced by using high-granularity detectors with good time resolution.

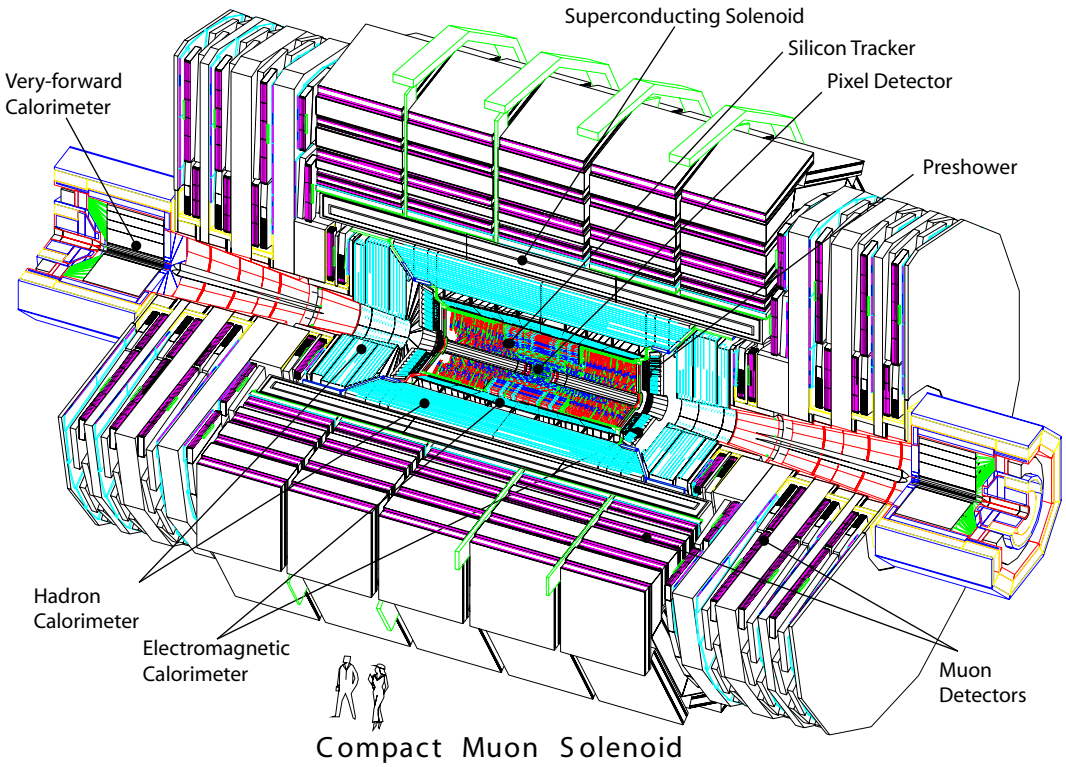

Figure 7: The CMS detector [3]

The coordinate convention sets the origin at the nominal collision point and the z-axis pointing along the beam direction, x-axis toward the center of the circle and the y-axis pointing up to the sky. There is also a special variable, the pseudorapidity $\eta = -\ln\tan(\theta/2)$, that is used to describe the polar-angle separation (see fig. 8). The momentum and energy measured transverse to the beam direction, i.e. in the xy - plane, are called p_T and E_T respectively and are computed using the x and y components.

An important aspect of the detector is the choice of the magnet, whose bending power is needed

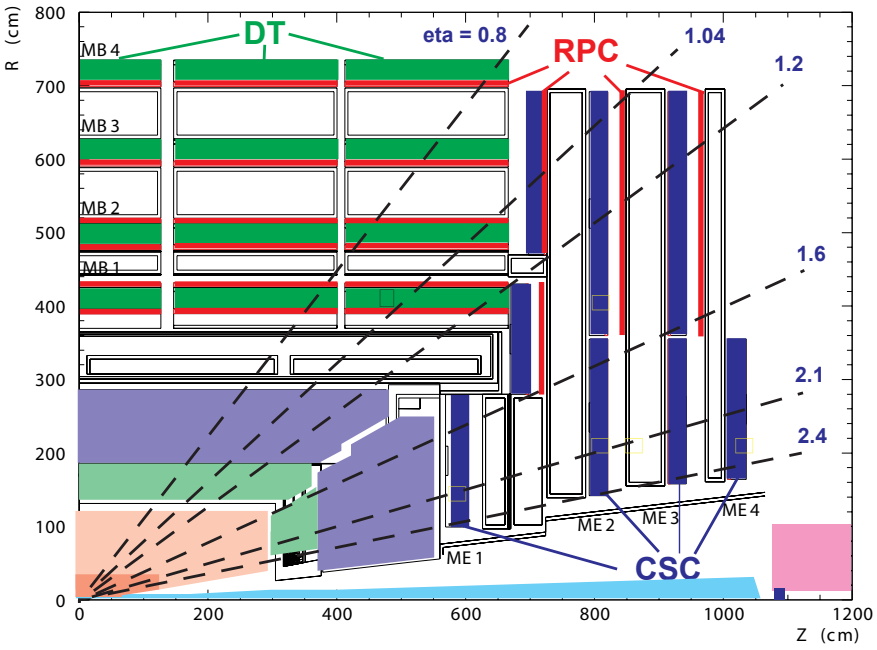

Figure 8: A longitudinal cut showing one quarter of the CMS detector (DT = drift tubes, CSC = cathode strip chambers, RPC = resistive plate chambers).

for precise measurement of the momentum of charged particles, foremost the muons. The 13-m-long, 5.9 m inner diameter, 4 T superconducting solenoid is stationed in the heart of the detector (see fig. 7). Outside the magnet are the muon chambers, consisting of several layers of aluminum drift tubes (DT) in the barrel region, cathode strip chambers (CSC) in the endcap region, and complemented by resistive plate chambers (RPC) as shown in figure 8. In total the muon system contains of order 25000 m^2 of active detection planes and nearly 1 million electronic channels.

Inside the magnet there is enough place for the inner tracker and the calorimetry system. There are ten layers of silicon microstrip detectors providing the required granularity and precision, and three layers of silicon pixel detectors placed close to the interaction region in order to improve the measurement there. The electromagnetic calorimeter (ECAL) is the next layer after silicon detectors. It is using lead tungstate crystals ($PbWO_4$) that have short radiation lengths, are fast and radiation hard. The ECAL is surrounded by the hadron calorimeter consisting of layers of brass and plastic scintillators. It is a conventional sampling calorimeter with a depth of about 5-10 nuclear interaction lengths.

2 Monte Carlo Samples

2.1 Production

All of the Monte Carlo samples used in this study were produced with the CMS software (CMSSW), version 2.1.10. The simulated unbiased pp collisions were generated by PYTHIA[4], version 6.416, using MSEL = 5 setting, that denotes the production of b-quarks via gluon-gluon fusion. The decays were produced by EvtGen[5]. The detector response to these physical processes was simulated using the fast parameterized simulation, FAMOS.

2.2 Data Sample

A large number of unbiased *pp*-collisions was produced to simulate real physical data. In order to reduce the amount of needed data, a preselection of the events was done on generator-level. A filter requiring the existence of two muons with certain properties was applied. Only events with two muons having a $p_T > 2.5$, $|\eta| < 2.5$ and a dimuon mass $m(\mu^+\mu^-)$ between 2.7 GeV and 3.5 GeV were accepted and then used in the reconstruction part of the analysis (see sec. 3.2).

About 3.34×10^9 events were generated and 4.23×10^8 of them passed through the filter. With a total *pp* cross-section $\sigma(pp \to b\bar{b}X) = 0.597$mb, that is used by PYTHIA instead of 0.500mb, the value of the integrated luminosity can be calculated as in the following formula:

$$\mathcal{L} = \frac{N_{gen.pp}}{\sigma_{pp}} = 0.708\,\mathrm{pb}^{-1}.$$

Note that at the design luminosity of $10^{34}\mathrm{cm}^{-2}$ per second $= 10\,\mathrm{nb}^{-1}$ per second $= 0.01\,\mathrm{pb}^{-1}$ per second, this amount would be achieved in 70,8 seconds.

2.3 Signal Sample

Because of the small branching fraction, $\mathcal{B}(B \to J/\psi(\to \mu^+\mu^-)K) = 5.98 \times 10^{-5}$, it would take too much time to produce enough data using just a filter requiring two muons that satisfy $p_T > 2.5$, $|\eta| < 2.5$ and $2.7\,\mathrm{GeV} < m(\mu^+\mu^-) < 3.5\,\mathrm{GeV}$ properties. For this reason a new sample containing only signal events was produced as well. In the first step the dimuon mass window was narrowed to $3.05\,\mathrm{GeV} < m(\mu^+\mu^-) < 3.15\,\mathrm{GeV}$, because only muons coming from a J/ψ, having a rest mass of 3.1 GeV, were required. Apart from this tightened dimuon filter, there was an additional constraint in the production. Since for the determination of the efficiencies and the differential cross-section only $B \to J/\psi(\to \mu^+\mu^-)K$ decay is of interest, this decay was forced, meaning that every time a B^+ or a B^- was produced, it was constrained to decay in the required way.

Applying the dimuon filter and forcing this decay, 10^6 events were produced. Though there are less produced events in this sample, there are more $B \to J/\psi(\to \mu^+\mu^-)K$ decay modes inside, because they were forced. For the calculation of the corresponding luminosity one should remember from section 1.2 the probability of the $b \to B^\pm$ process to be 0.4, or $0.4^2 = 0.36$ for the $b \to B^+B^-$ process. That means that the probability for both *b*-quarks to produce any other decay is 0.64 and should be incorporated in the calculation of the luminosity for this sample. Another correction factor is the branching fraction, that is used to represent the real number of *pp*-collisions needed to produce such an amount of $B \to J/\psi(\to \mu^+\mu^-)K$ decays as there are in this sample. Putting all together one gets the following formula:

$$\mathcal{L} = \frac{N_{gen.pp} \times 0.64}{\sigma_{pp} \times \mathcal{B}}.$$

Using the values above, the luminosity becomes $17.920\,\mathrm{pb}^{-1}$. This integrated luminosity value corresponds to a running time of approximately 30 minutes for the LHC.

3 Event Reconstruction

3.1 Signal Signature

The data consists of many different decays, therefore the knowledge of the decay process of $B^+ \to J/\psi(\to \mu^+\mu^-)K^+$ must be used for its identification. As shown in figure 9, the B meson decays nearly immediately into a J/ψ and K, and the J/ψ afterward into a $\mu^+\mu^-$ pair. So both muons

and the kaon are the only particles which can be measured and used for the reconstruction of the B-meson. As described in section 1.4 the muons can be recognized in the muon chambers, because they are the only particles that have enough energy to pass through all the other detectors and make at least one hit in the chambers. Of course not only muons coming from a B-meson are detected in the chamber, but also muons coming from other decays. So the challenge is to find the pair that really belongs to the J/ψ coming from a B-meson.

The kaon can not be identified in the detector, because it is just measured as a charged particle with a certain amount of energy, which also could have been a proton or an other charged hadron. So one has to try different kaon candidates in order to possibly find the right one.

After having found these three particles, the whole process can be reconstructed. Both muons should have an invariant mass of a J/ψ particle and the tracks of both muons and the kaon should lie relatively close of each other because of the boost, meaning that once those tracks are reconstructed, the K track should be searched in the neighborhood.

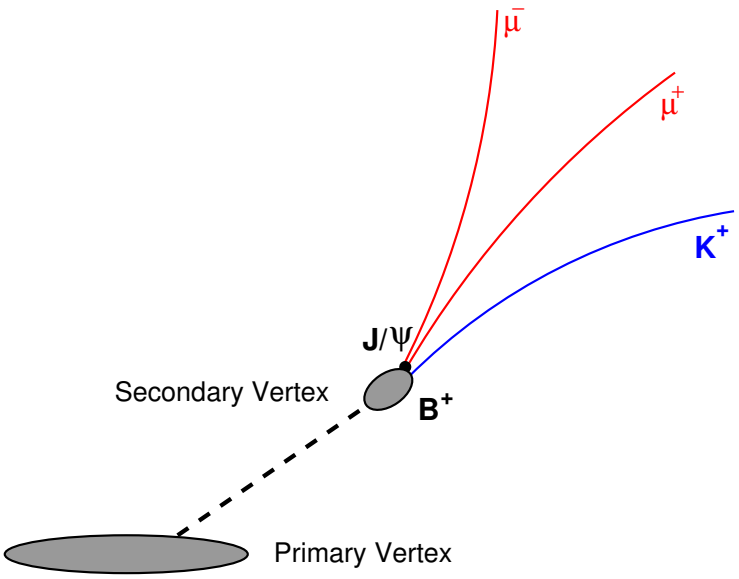

Figure 9: Signal topology

3.2 B Reconstruction

As already mentioned, two muon tracks and a kaon track are required in order to reconstruct a B-candidate. In order to understand how difficult this task could be one should take a look on figure 10. In this figure the number of tracks per event is plotted. Out of the statistic box one can see that the mean value is approximately 61 tracks per event. That means that these three track should be chosen out of, on average, 61 tracks.

The reconstruction is started with a muon track and then continued with the search for another one having the opposite sign. On figure 11 one can see the number of muons that can be found in an event. Mostly there are two of them, but also four, five or even more can be found. The transverse momentum of both muons has to be bigger than 2.5 GeV in order to ensure that both of them are able to reach at least the first muon chamber.

After building the four-momentum vector of the J/ψ out of the muons, the next cut is applied:

only muon pairs with an invariant mass around J/ψ mass are accepted. This cut is quite loose, which implies several possible candidates per event. In the next step, a third reconstructed track is chosen as a candidate for K. Fulfilling a p_T cut of 1 GeV, there are 19 tracks on average that could be possible candidates for the kaon (see fig. 12). Therefore the angular separation of the J/ψ and K is used as another criteria to reduce this number. After a K candidate is chosen, it can be used together with the J/ψ to build the B candidate, which should fulfill a mass cut in order to ensure its mass to be not far away from the expected B-mass of 5.279 GeV.

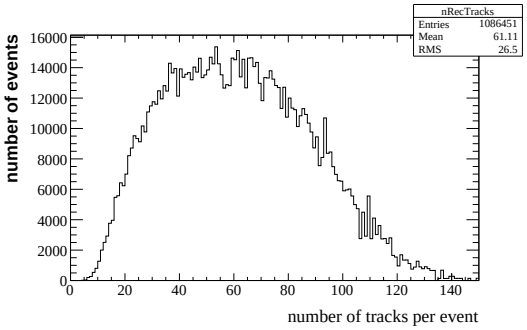

Figure 10: Number of tracks per event

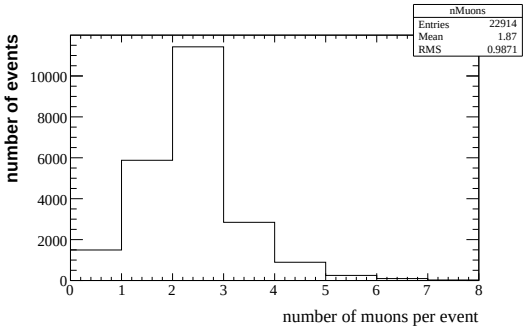

Figure 11: Number of muons per event

Using this candidate reconstruction method, up to 20 candidates can be found in an event (see fig. 13). On average there are 4 – 5 candidates in each event, meaning that some additional properties should be used to filter out the right one. Note that there is also the possibility that none of the reconstructed candidates is right, because a muon or the kaon could have been lost.

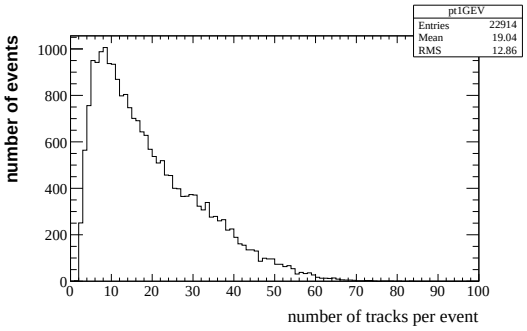

Figure 12: Tracks with $p_T > 1\,\mathrm{GeV}$

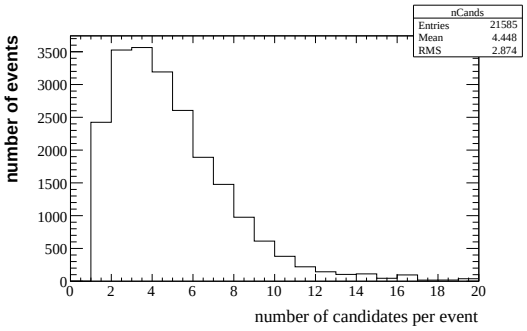

Figure 13: Number of candidates per event

In the analysis all of the mentioned criteria are tightened and some additional criteria are used to sort out the "bad" candidates already at the beginning. So for example $\Delta R = \sqrt{\Delta\phi^2 + \Delta\eta^2}$ is used to constrain the K-candidate to be inside a cone defined by the momentum vector of the J/ψ. The new criteria are put together in the list below:

- Muon track:
  - $p_T(\mu) > 3.0\,\text{GeV}$
  - $|\eta(\mu)| < 2.4$
- $\mu^+\mu^-$-system:
  - $3.0 < m(\mu^+\mu^-) < 3.2\,\text{GeV}$
- Kaon track:
  - $p_T(K) > 2.0\,\text{GeV}$
  - $|\eta(K)| < 2.4$
  - $\Delta R(J/\psi, K) < 1.2$
- $\mu^+\mu^- K$-system:
  - $5.0 < m(\mu^+\mu^- K) < 5.5\,\text{GeV}$

As one can see from this list, the p_T cut for the muons has been increased from 2.5 GeV to 3 GeV. On the figures 14 and 15 one can see the p_T distribution of both muons after the $p_T > 2.5\,\text{GeV}$ cut, and the relative reduction factor due to the enhancement of the cut-level to 3 GeV. Taking the number of muons present after the 2.5 GeV cut as 100 % and applying the new cut on the remaining particles, one cuts off approximately 7 % of the muons.

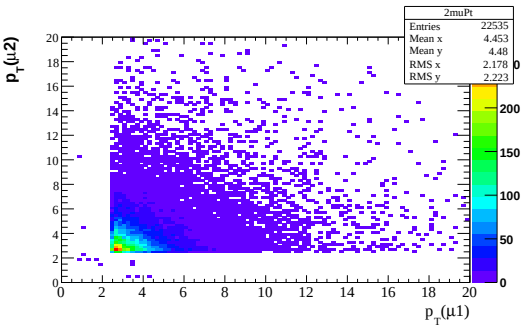

Figure 14: p_T distribution of both muons

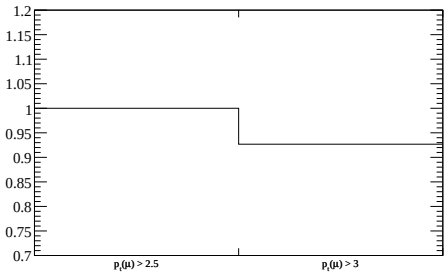

Figure 15: Reduction factor for muons

After the construction of the candidate, its information is stored in a structure containing indices and three-momenta of both μ-tracks and the K-track. Further it also contains the mass, three-momentum and vertex-properties of the B candidate. Moreover the tracks of μ's and K are refitted before storing using the B-vertex in order to improve them.

3.3 Candidate Selection

Using the reconstruction method described in the last section one gets on average $4-5$ B-candidates per event instead of one single B. Since the probability of getting two $B \to J/\psi\,(\to \mu^+\mu^-)K$ decays in the same event is of order $((1.008 \times 10^{-3}) \times (5.93 \times 10^{-2}))^2 \approx 3.6 \times 10^{-7}\,\%$, in this analysis only one candidate per event should be chosen for later tests. This implies a search for an appropriate selection criteria, in order to keep the background as small as possible.

The idea is to consider different physical properties of good candidates ("signal") and bad candidates ("background"). The "signal" corresponds to a $B \to J/\psi(\to \mu^+\mu^-)K$ decay, whereas "background" means $B \to J/\psi(\to \mu^+\mu^-)X$. In the following figures 16 – 25 some of these properties are compared. Most of these figures represent distributions of some kinetical or spatial properties of the involved particles, such as the transverse momentum p_T or the pseudo rapidity η. Furthermore there is also $\Delta R^(J/\psi, K)$ and mass plots of J/ψ and B-candidate. Apart from these obvious dependences one more is considered: the χ^2 value of the B-candidate vertex.

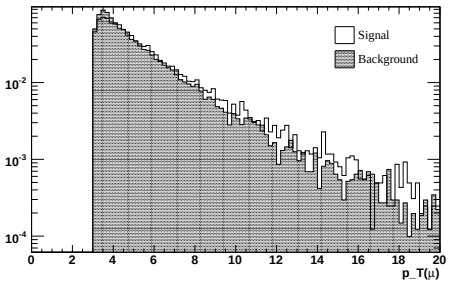

Figure 16: $p_T(\mu)$

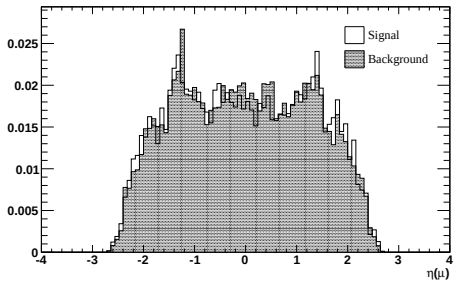

Figure 17: $\eta(\mu)$

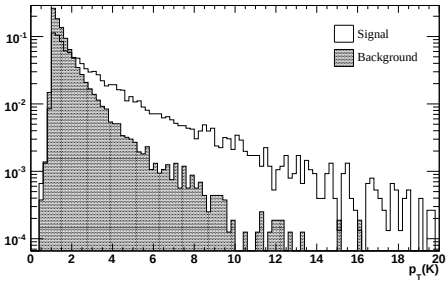

Figure 18: $p_T(K)$

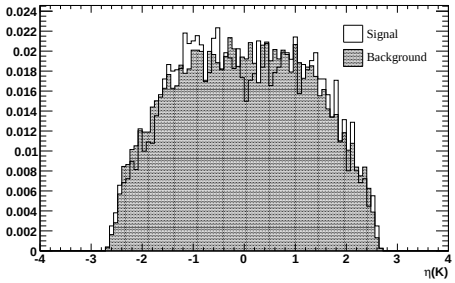

Figure 19: $\eta(K)$

All these properties could be used in order to enhance the purity of the chosen candidates. In this case the purity stands for the relative number of true candidates out of all chosen candidates and the goal is to make it as high as possible. Therefore, an adequate property should be chosen to cut off as much background as possible, simultaneously leaving good candidates unaffected. Most of the plotted distributions are not suitable for such a cut, so the $p_T(\mu)$, $\eta(\mu)$, $p_T(K)$, $\eta(K)$, $\Delta R(J/\psi, K)$, p_T (B) and $\eta(B)$ can not be used because the difference in the shapes of signal and background is so tiny that there is no possibility to cut off background without loosing signal. The dimuon mass $m(\mu^+\mu^-)$ is already implemented as a cut constraining the mass to the 3.0 GeV– 3.2 GeV window around the J/ψ mass-peak. The $m(B)$ cut is also already used to only let through candidates with a mass between 5.0 GeV– 5.5 GeV, but in figure 22 one can easily recognize that

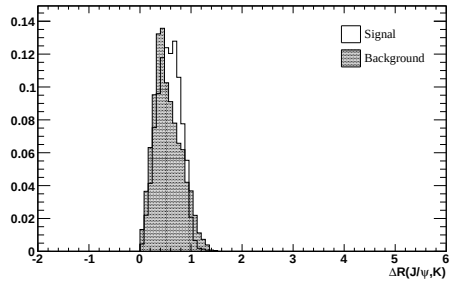

Figure 20: $\Delta R(J/\psi, K)$

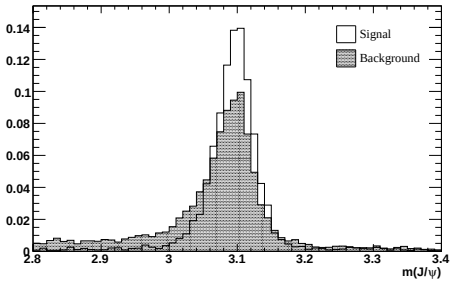

Figure 21: $m(\mu^+\mu^-)$

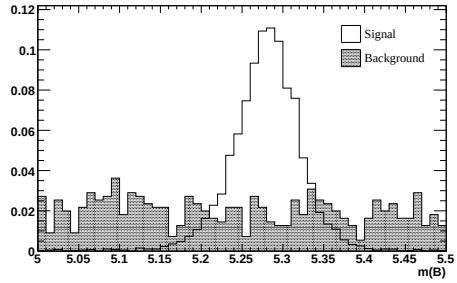

Figure 22: $m(\mu^+\mu^- K)$

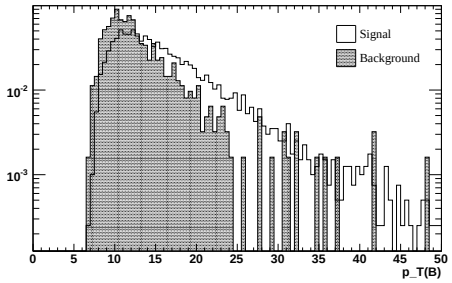

Figure 23: $p_T(B)$

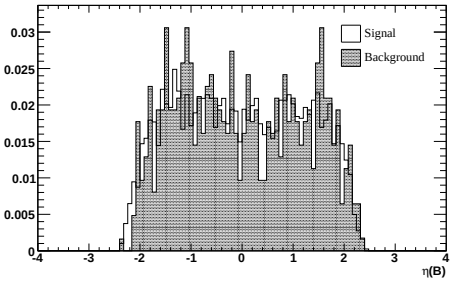

Figure 24: $\eta(B)$

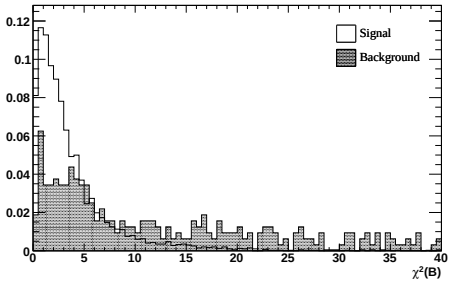

Figure 25: $\chi^2(B)$

for values smaller than 5.15 GeV and bigger than 5.4 GeV the background predominates clearly. So later only candidates with a mass between 5.15 GeV and 5.4 GeV shall be accepted as true candidates.

Another value which could be used to enhance the purity is the $\chi^2(B)$. As shown in figure 25 the signal has a peak that is concentrated near the zero value and the background is less concentrated, but has a longer tail. So one could claim the candidate with the smallest χ^2 value to be the true one, because the probability of having chosen the right candidate is bigger for smaller χ^2 values than for bigger ones. Further one should notice that signal and background curves cross at a χ^2 value of approximately 5. Beyond this value there is always more background than signal and

therefore it would be possible to cut off the long tail, getting rid of a lot of background and loosing only few signal events.

This χ^2 cut is applied after all the other cuts, i.e. after the most background events have been excluded. In the following figure 26 the χ^2 distributions of remaining signal and background events from data sample are shown. The use of the logarithmical scale in figure 27 allows to better compare both distributions and decide, which value would be suitable for the cut. Beyond a χ^2 value of 15 there are almost only background events, so out of this figure a $\chi^2 = 15$ cut could be chosen.

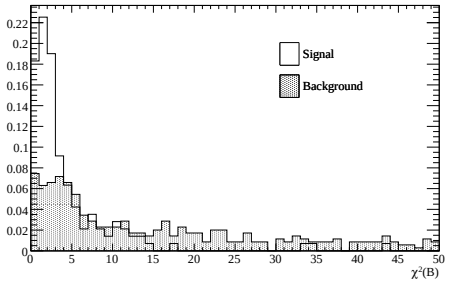

Figure 26: χ^2 distribution before cut

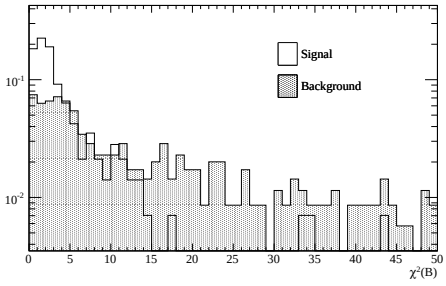

Figure 27: χ^2 distribution before cut (logarithmical scale)

Considering the purity as a function of the χ^2 cut (see fig. 28) one can easily realize, that the best purity value is achieved for a χ^2 value near by zero. The bigger the cut is chosen, the lower becomes the purity. For big χ^2 values it converges to the purity-value without any cut, i.e. approximately 0.19. The task to choose the right cut-value out of this or previous figures is not so easy as is seems, because a near-zero cut leads not only to a high purity, but also to a big signal loss. That is why the significance of the events has to be used for the determination of the appropriate cut-value. The significance is defined as:

$$\sigma = \frac{S}{\sqrt{S+B}},$$

where S denotes the number of true signal events and B the number of true background events in the data sample (see fig. 29). The best cut-value is the one with the biggest significance value, and therefore a χ^2 cut of approximately 13 should be chosen in order to enhance the purity without loosing too much signal events. From figure 28 one can determine the purity corresponding to $\chi^2 = 13$ to be 0.4. This value seems to be quite low, but one should remember that it is computed for the whole 5.0 GeV– 5.5 GeV region. Constraining the candidate-mass to the 5.15 GeV– 5.4 GeV window, one gets a different purity dependence (see fig. 30), and a purity value of almost 0.6 for $\chi^2 = 13$.

3.4 Fitting Signal Peaks

After having applied all cuts to the candidates, there are only few of them left, being more precise: not more than one per event. But, despite these constraining cuts, there are still some background events. The best way to see it is to cast the masses of all remaining B-candidates into a histogram

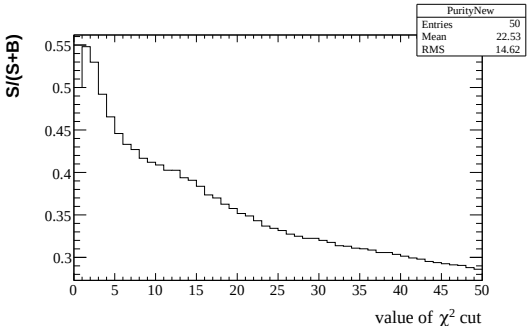

Figure 28: Purity of the selected B-candidates

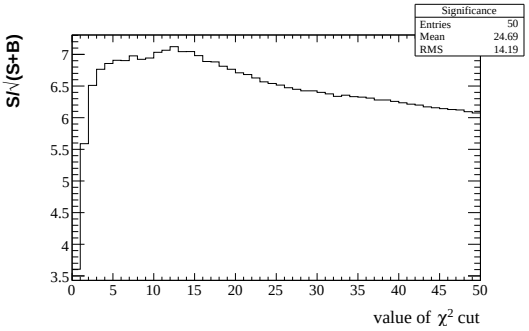

Figure 29: Significance of the events

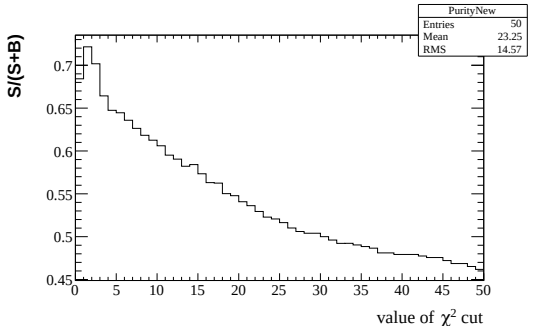

Figure 30: Purity for candidates in the 5.15 GeV– 5.4 GeV window

(see fig. 31). All of the true candidates have a mass near the 5.279 GeV value; false candidates have no peak at this value and are distributed over all region. So the way to determine the number of true candidates is to count the events in the peak surrounding the B rest mass. Though there are only 313 events filled in the histogram, a peak around 5.279 GeV is very clear. In order to find out how many signal events there really are, one has to use some fitting function and separate signal events from background. There are different approaches for such a fitting function. One of them is presented below.

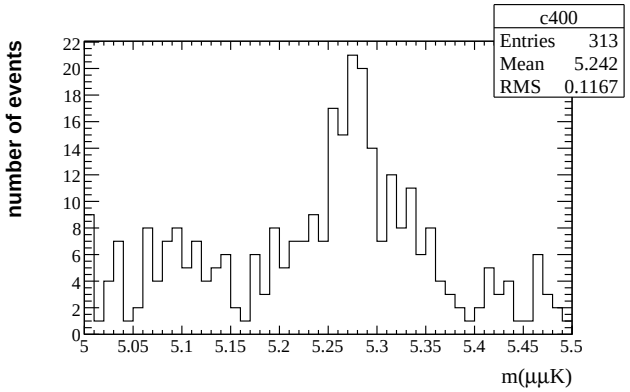

Figure 31: Distribution of B-candidates' masses

3.4.1 Gaussian Fitting

Looking at figure 31 one can make the straightforward attempt to use a linear polynomial for the background fit and combine it with a gaussian fit for the peak. Adding these functions together the fitting function becomes:

$$f_{fit}(x) = f_{backgr.}(x) + f_{signal}(x) = p_0 + p_1 x + p_2 \exp\left(-\frac{(x-p_3)^2}{2\,p_4^2}\right),$$

where $p_0, \ldots p_4$ are the fit parameters. In order to ensure the fitting procedure to be stable, i.e. to produce appropriate fitting functions, the parameters were initialized at estimated starting values:

- p_0 (Initial value of the linear polynomial)
  - The initial value for the linear polynomial is computed as the average of the first five bins of the histogram in order to minimize the error.
- p_1 (Slope of the linear polynomial)
  - The slope of the linear polynomial is estimated using the first and the last five bins of the histogram, and is equal to the ratio of its difference and the x-range of the histogram.
- p_2 (Amplitude of gaussian)
  - The amplitude value of the gaussian peak was set to be the maximum entry of the histogram minus the value of the background shape at this point, that was calculated using the initial fitting values of the linear polynomial.
- p_3 (Mean value of gaussian)
  - The mean value of the gaussian peak was chosen to be at the rest mass of the B-meson (5.279 GeV)
- p_4 (Width of gaussian)
  - The width of the gaussian was set to 0.05 GeV.

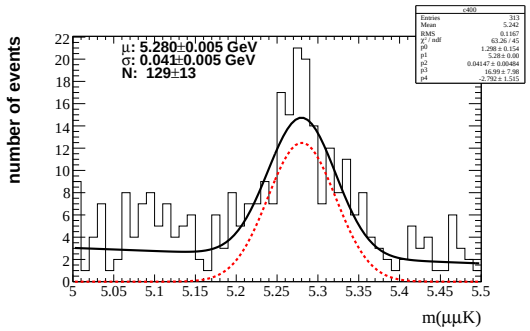

Figure 32: Fitted B-candidate mass

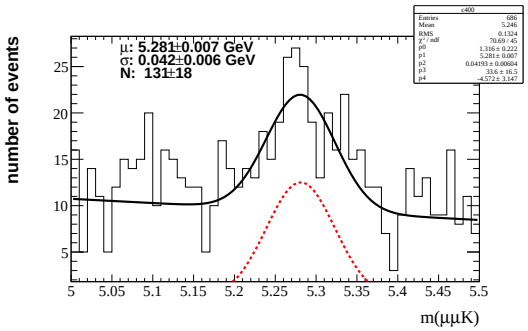

Figure 33: Fitted B-candidate mass before χ^2 cut

Using these parameters and the upper fitting function, one gets a fit as in figure 32. One can clearly see the linear background that is slightly descending toward higher mass values, and a peak with the mean value at 5.28 GeV. In order to be sure that only few true candidates were lost due to the χ^2 cut, one can look at the same figure before the cut was applied (see fig. 33). It is striking out that there are much more background events: the total number of events in the plot is 686, i.e. more than twice as big. However the number of signal events in the peak is approximately the same, so one can conclude that only very few true candidates were lost due to the cut. The reduced amount of background leads to a more accurate determination of the signal event number, because the error of the integral over the peak becomes smalles. Thus the total error of the analysis is reduced.

3.4.2 Double Gaussian Fitting

In other parts of the analysis, a different fitting function may be more appropriate. For instance there are several functions that look gaussian but have some sort of tails, that can not be fitted using just a single gaussian function. One possibility to account for multiple widths, is to use a superposition of different gaussians as a fit-function, so the new fitting function for such signal shapes would be:

$$f_{signal}(x) = p_2 \exp\left(-\frac{(x-p_3)^2}{2\,p_4^2}\right) + p_5 \exp\left(-\frac{(x-p_6)^2}{2\,p_7^2}\right),$$

where there are now 6 fitting parameters (p_0 and p_1 are reserved for the linear background). Combined with the background fitting function one gets as the result:

$$f_{fit}(x) = p_0 + p_1 x + p_2 \exp\left(-\frac{(x-p_3)^2}{2\,p_4^2}\right) + p_5 \exp\left(-\frac{(x-p_6)^2}{2\,p_7^2}\right).$$

3.4.3 Resolutions of p_T and η

Another interesting property of the analysis is to find out how precisely the required values of p_T or η can be determined. Because these values are used in the determination of the best candidate, the precision of its measurements makes the analysis more or less accurate. For this reason, three properties have been studied:

- the transverse momentum p_T
- the inverse transverse momentum $\frac{1}{p_T}$
- the pseudorapidity η.

For the reconstruction of J/ψ and B-candidate the p_T-values of the $\mu^+\mu^-$ pair and of the K candidate are used, and thus contribute to the imprecision of this reconstruction. For this reason, the above properties have been first studied generally for all tracks, and then for the both reconstructed particles B and J/ψ in particular. In order to find the resolution, the difference of the reconstructed and generated values was plotted. Assuming the reconstruction process to be quite accurate, one should expect these plots to be quite narrow and to have a peak at zero. In the figures 34 – 36 one can see the distributions of p_T, $\frac{1}{p_T}$ and η for all tracks fitted using a double gaussian function described in section 3.4.2. In each histogram the mean value μ and the standard deviation σ are displayed. The mean values of all three plots are approximately at zero, confirming the expectation on the distribution. The deviations of the gaussians give back the resolutions of

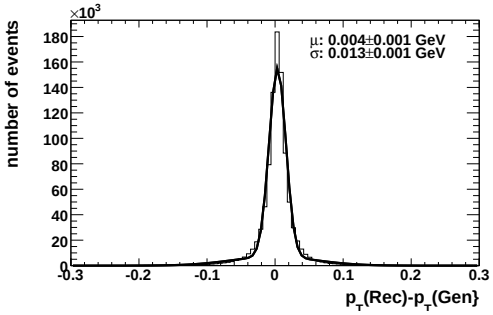

Figure 34: Resolution of p_T (Track)

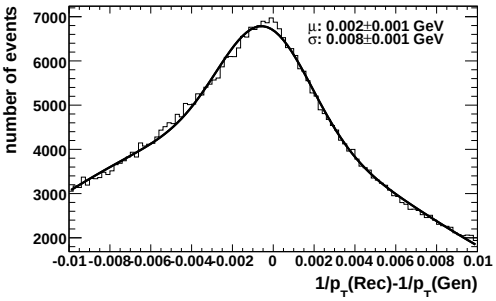

Figure 35: Resolution of $\frac{1}{p_T}$(Track)

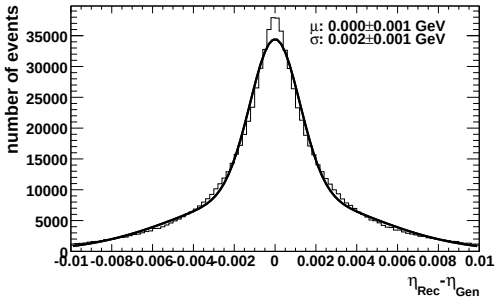

Figure 36: Resolution of η(Track)

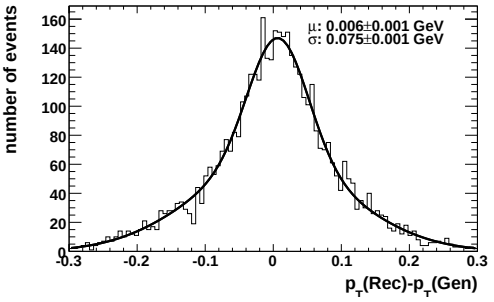

Figure 37: Resolution of p_T (J/ψ)

the kinematical properties of the tracks, so for example out of the plot 34 one can read out that the p_T value of a track can be determined up to an error of 0.013 GeV.

After the resolutions for the tracks have been determined in general, one can step further to the reconstructed particles of the decay chain: J/ψ and B. In figures 37 – 42 the corresponding histograms are shown. As one can see from the double gaussian fit in figures 38, 39, 41 and 42, these distributions have a standard deviation of approximately 0.001, so one can follow that the resolutions of the η and $\frac{1}{p_T}$ values of the particles are very good. The transverse momentum value p_T for J/ψ and B has a less exact form but still can be fitted using a double gaussian function. However the distribution is broader and thus results in a bigger σ value: 0.075 GeV for J/ψ and 0.094 GeV for the B meson.

As the goal of this thesis is to determine the differential cross-section, i.e. the dependence of the cross-section on p_T value of the B-candidate, it is interesting to find out how the resolutions of the transverse momentum, its inverse and the pseudorapidity are changing with p_T or respectively η. In figures 43 - 48 these dependences are shown. The η dependence of the resolution look similar for the tracks, J/ψ and B (see fig. 44, 46, 48). The resolution is best around the $\eta = 0$ value and double its value toward higher $|\eta|$-values. The plots for the p_T resolution dependences for J/ψ and B are also similar (see fig. 45 and 47). Here the resolution stays approximately at the same value for the whole p_T region. The only property showing another behavior is the p_T value of the tracks (see fig. 43). In order to better illustrate its resolution dependence, the errors of each value have been filled in an additional plot (see fig. 49). It starts at approximately 0.04, then gets a little bit down to 0.025 and then rises again toward higher p_T-values up to nearly 0.1. The reason for the rise toward higher p_T-region is multiple scattering and energy loss due to ionisation in the material of the detector; higher uncertainty for low p_T-region arises because its curvature (determined by the magnet field), which is used for the p_T determination, is very small and can not be measured well.

4 Measurement of Differential Cross-Section

The main goal of this thesis is to determine the differential cross-section of the $pp \to B^+X \to J/\psi(\to \mu^+\mu^-)K^+X$ decay. This can be done using the following formula for the differential cross-section:

$$\frac{d\sigma_{B^+}}{dp_T(B^+)} \times \mathcal{B}(B^+ \to J/\psi K^+) \times \mathcal{B}(J/\psi \to \mu^+\mu^-) = \frac{N(p_T)_{B^+_{prod.}}}{\mathcal{L} \times \Delta p_T} = \frac{N(p_T)_{B^\pm_{reco.}}}{2 \times \epsilon_{tot.} \times \mathcal{L} \times \Delta p_T},$$

where by $N(p_T)_{B^+_{prod.}}$ is meant the produced number of B^+-mesons decaying in to a J/ψ ($\to \mu^+\mu^-$) and a K^+, and by $N(p_T)_{B^+_{reco.}}$ the reconstructed number of these decays. As one can see from this formula there are several components that have to be determined. First there is the integrated luminosity, that can be estimated from the number of generated events and the total pp cross-section. Substituting in the numbers of section 2.3, the integrated luminosity becomes:

$$\mathcal{L} = \frac{N_{gen.pp} \times 0.64}{\sigma_{pp} \times \mathcal{B}(B \to J/\psi(\to \mu^+\mu^-)K)} = 17.920\,\mathrm{pb}^{-1}.$$

Also the number of events with a certain transverse momentum, $N(p_T)$, is important for the differential cross-section. This number is assumed to be the number of $\mu^+\mu^-K$ originating from

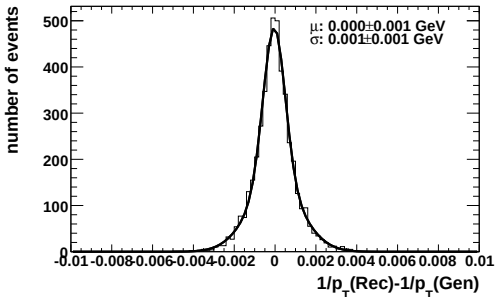

Figure 38: Resolution of $\frac{1}{p_T}(J/\psi)$

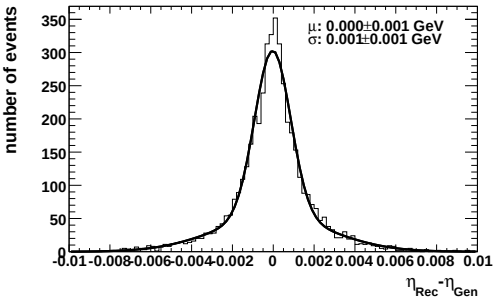

Figure 39: Resolution of $\eta(J/\psi)$

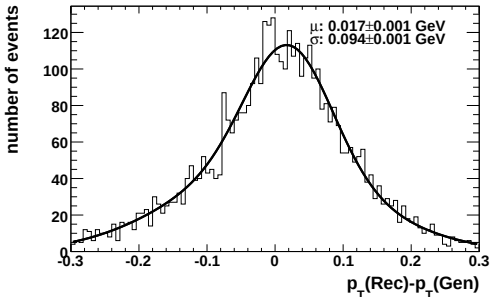

Figure 40: Resolution of p_T (B)

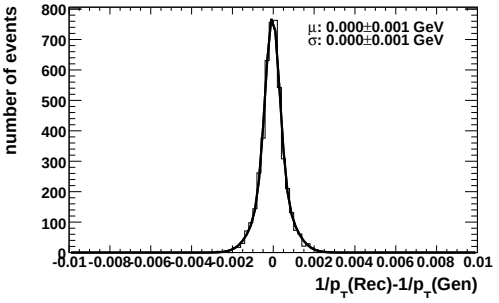

Figure 41: Resolution of $\frac{1}{p_T}(B)$

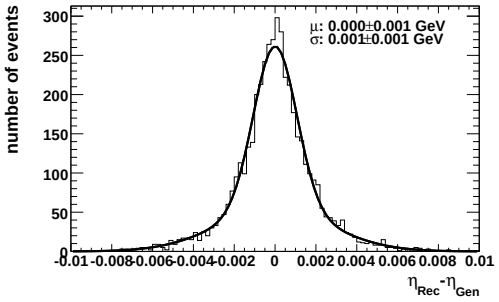

Figure 42: Resolution of $\eta(B)$

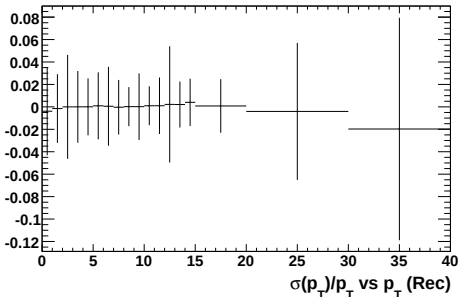

Figure 43: Resolution of p_T (Track) as function of p_T (Track)

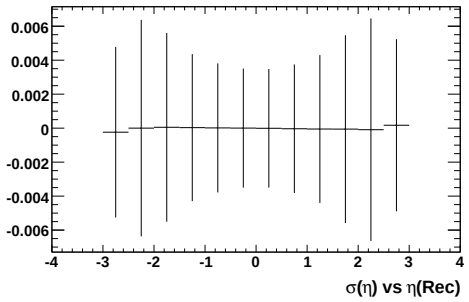

Figure 44: Resolution of η(Track) as function of η(Track)

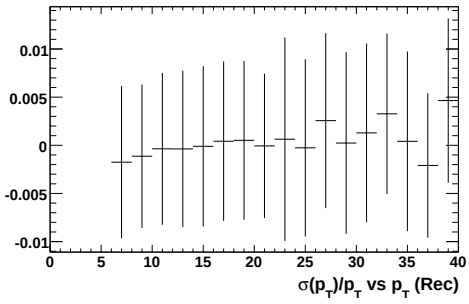

Figure 45: Resolution of η(Track) as function of p_T

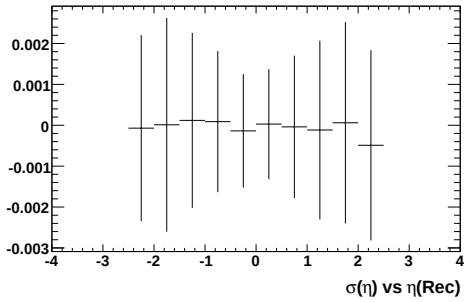

Figure 46: Resolution of $\eta(B)$ as function of $\eta(B)$

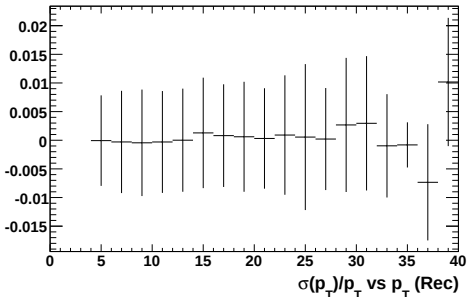

Figure 47: Resolution of p_T (J/ψ) as function of p_T (J/ψ)

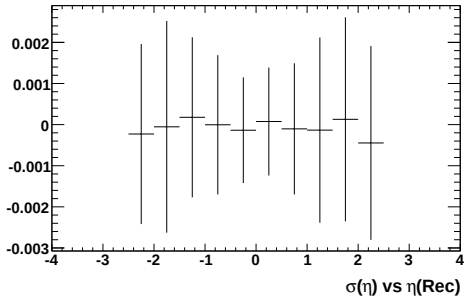

Figure 48: Resolution of $\eta(J/\psi)$ as function of $\eta(J/\psi)$

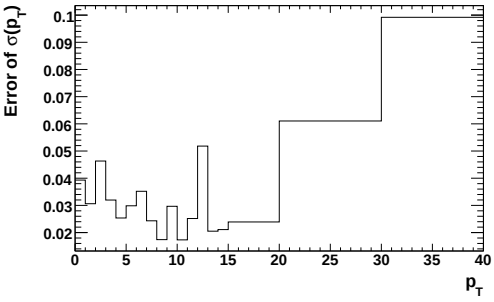

Figure 49: p_T dependence of the error on p_T-resolution of tracks

a B-meson passed through all cuts, and can be determined using the method described in section 3.4. Because of the cuts applied for the reduction of background events, the number of totally reconstructed candidates is reduced after each step. That is why it is important to pay attention to all efficiencies and acceptance factors during the analysis. All these factors can be put together and are denoted by $\epsilon_{tot.}$ in the formula.

The factor 2 is included because not only B^+ are used for the determination of the differential cross-section, but also B^-. The total number of $B^\pm$ hence has to be divided by 2 in order to get the number of B^+.

4.1 Transverse Momentum Binning

In order to be able to compute the differential cross-section $d\sigma/dp_T$ one has to find first the number of events having a certain transverse momentum as function of this momentum: $N(p_T)$. In figure 50 the candidates are filled into the histogram according to their p_T-values, forming a distribution that decreases toward low and high p_T-values and has a peak around 11 GeV. This shape leads to an inaproppriate partitioning of $N(p_T)$: so for example the number of events with a p_T-value between 5 GeV and 6 GeV is zero, whereas the number of events within the 10 GeV–11 GeV window is more than 400. Because of such differences, a new binning with variable bin widths should be chosen to get comparable amount of events in each bin. In table 2 this binning is shown.

Table 2: Binning

Bin	1	2	3	4	5
Range / GeV	0-10	10-11	11-12	12-13	13-14
Bin width / GeV	10	1	1	1	1
Bin	6	7	8	9	10
Range / GeV	14-15	15-17	17-19	19-23	23-60
Bin width / GeV	1	2	2	4	37

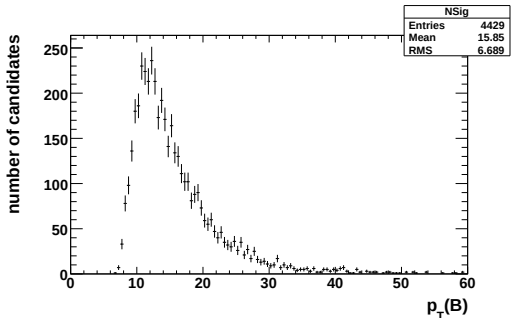

Figure 50: Number of B-candidates as function of p_T

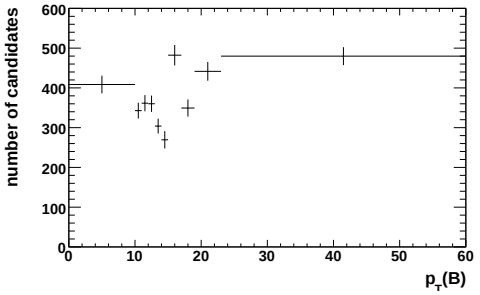

Figure 51: $N(p_T)$ with new binning

4.2 Fitting the Peaks

Using the binning above, the events are cast in ten histograms, each covering a certain $p_T(B)$ range of table 2. The new binning guarantees that in every bin there is a similar number of events as in others, and thus the same fitting function can be applied. In the signal sample there is almost no background present, but the histograms are nevertheless fitted with the combined fitting function as described in section 3.4.1 in order to get the precise number of events in the peak (see fig. 52). Out of the fit, the integral over the gaussian function is calculated, and the number of B-candidates is determined. For the signal sample this number is approximately equal to the total number of events filled in the histogram (because nearly no background events are presented), but the proper data, that will be considered later, contains much more background events and there the number of the candidates in the peak will differ from the total number (see section 5.2). After all histograms have been fitted, the numbers of the events in their peaks are filled in a new histogram (see fig. 51), combining the results out of all ten histograms together. The errors in this new histogram are computed out of the fitting function errors and also stored in the new histogram for later use.

4.3 Efficiency Determination

As already mentioned, not all of the produced B-candidates can be accounted for the determination of the differential cross-section, because only a part of them can be reconstructed and only some of them pass through all cuts used for the determination of the best candidate. In order to reconstruct the total number of produced B-candidates all of these reduction factors have to be calculated.

4.3.1 Muon Acceptance

Using PYTHIA, a certain amount of pp collisions were generated and then checked on whether they are suitable for the analysis or not. The idea was to choose events with a pair of muons, each having a transverse momentum of at least 3 GeV. This value corresponds to the dimuon trigger value, which is used in the experiment in order to make sure, that both muons reach at least the first muon chamber. There are also limits for the spatial angular acceptance of the detector, therefore only muons with $|\eta(\mu)| < 2.4$ were accepted. In order to find the muon acceptance, that arises due to these two limitations, one has to produce two plots: all generated muons (see fig. 53) and all muons that fulfill both limiting conditions (see fig. 54). The muon acceptance is then the ratio of reduced values and the full amount of generated muons (see fig. 55).

4.3.2 Muon Identification Efficiency

In the detector a muon is identified by matching a sequence of hits (or even one single hit) in the muon chambers with corresponding sequence of hits in the tracker and pixel detector. This method is therefore successful, as muons are the only particles which are expected to reach the muon chambers. All of the other particles should be absorbed in the ECAL, HCAL (see section 1.4) or the material in-between. Misidentifications arise for muons with a low p_T which is not large enough to reach even the first muon chamber, and therefore can not be identified as a muon. The reason for this is energy loss due to ionization and atomic excitation that the muon suffers as it crosses the detector material. So the mean distance a muon can travel inside the detector depends linearly its momentum. Another source of impurity are high energetic pions and kaons that manage to cross the distance to the muon chambers, produce hits and therefore to be identified as muons.

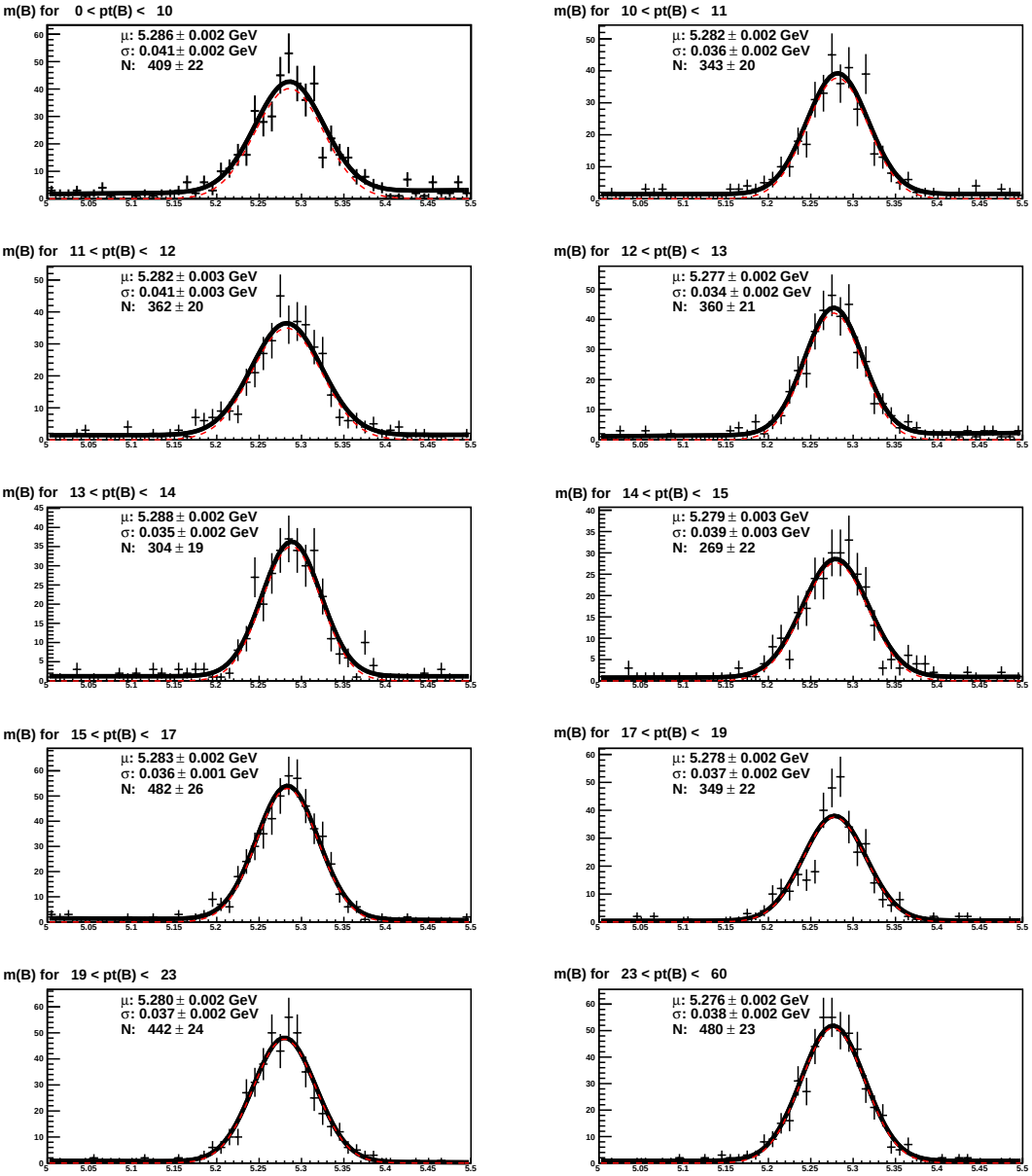

Figure 52: Mass distribution of candidates within different p_T-windows

For the analysis it means that, in contrary to the muon acceptance, which was studied using only generator information, for the muon identification efficiency the reconstruction information is important. By muon identification efficiency is meant the ratio of "muons reconstructed as muon" and "muons reconstructed as muons + muons reconstructed as something else". For this purpose all reconstructed muons and all generated muons were filled in a 2D histogram (see fig. 56 and fig. 57). Dividing these two histograms one get the efficiency of reconstructing a muon with certain p_T and η values (see fig. 61). Notice that the identification efficiency is nearly 100 % everywhere

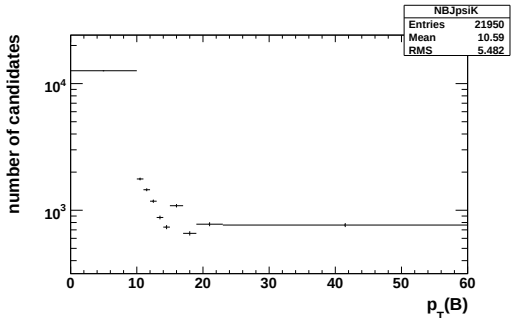

Figure 53: Total generated number of candidates

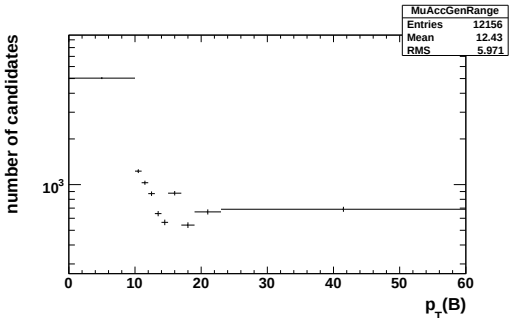

Figure 54: Generated number of candidates having both muons in the acceptance region

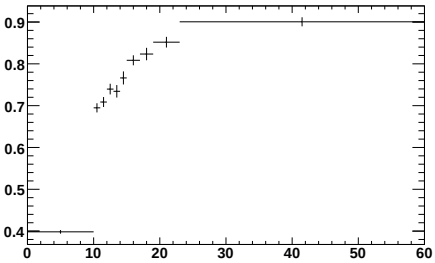

Figure 55: Muon Acceptance

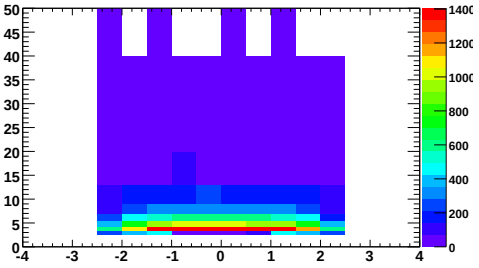

Figure 56: Reconstructed muons in the acceptance region

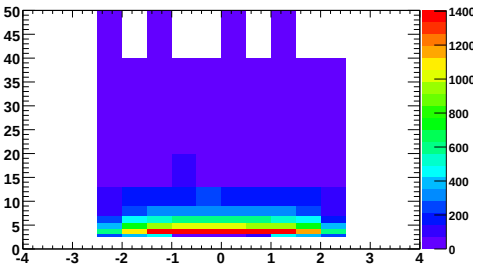

Figure 57: Generated muons in the acceptance region

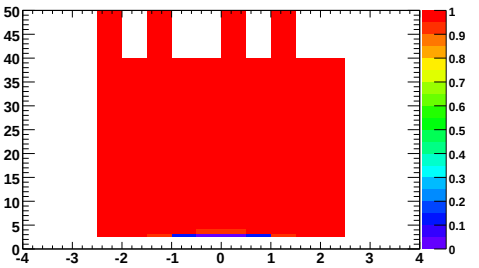

Figure 58: Ratio of muons reconstructed as muons and all generated muons in the acceptance region

beside the region with low p_T-values. In figure 59 the misidentification rates of muons as pions and of pions as muons are shown. Further, plotting the p_T-values of the 6 % misidentified muons (see fig. 60), one can clearly recognize that most of them have a low p_T-value, which confirms the expectation on low p_T muons to not have enough energy to reach even the first muon chamber.

After this relation had been found, the muons coming from a B-candidate were considered in

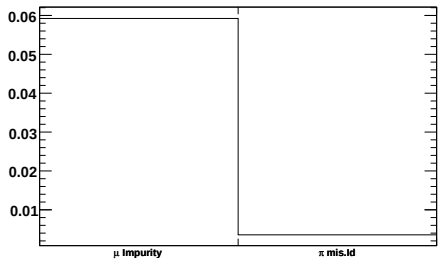

Figure 59: Muon impurity and pion misidentification rate

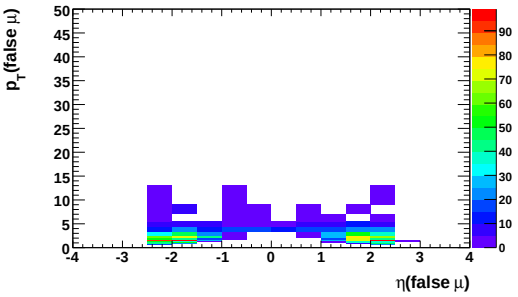

Figure 60: p_T distribution of muons reconstructed as pions

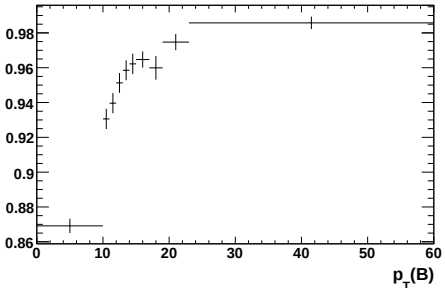

Figure 61: Muon identification efficiency

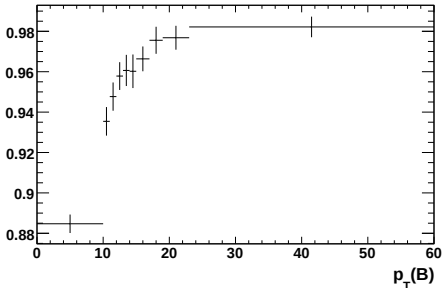

Figure 62: J/ψ efficiency

order to find the limitation factor for the analysis. Such a muon was located on the histogram 58, and its reconstruction efficiency value was then multiplied with the value from the second muon, after it had been located too. Doing this for all B-candidates, the muon reconstruction efficiency could be filled in a new histogram (see fig. 61) as function of the p_T-value of the B-candidate.

4.3.3 m(J/ψ) Cut

After both muons were found, they were used for the reconstruction of their mother particle — the J/ψ. Out of the combination of their four momenta, the invariant mass could be found and then used as another cut. Remembering the J/ψ mass to be 3.1 GeV, one only let pass through muon pairs with an invariant mass between 3.0 GeV and 3.2 GeV. The efficiency starts at 0.88 and rises to 0.98 for bigger p_T-values (see fig. 62).

4.3.4 Kaon Acceptance

As explained in section 3.1 concerning the reconstruction of the B-meson, after having found two muons inside the muon acceptance region, a kaon candidate should be chosen. Similar as for the muons, there is an acceptance range for the kaon, that has to be kept in mind for the determination of the differential cross-section of the decay. For the kaon there is the same angular acceptance of $|\eta| < 2.4$, but a different cut for the transverse momentum: only kaons with $p_T > 2$ GeV are accepted for the analysis. For the determination of the kaon acceptance the ratio of "generated kaons fulfilling both acceptance conditions" and "full range of kaons" was calculated and then used

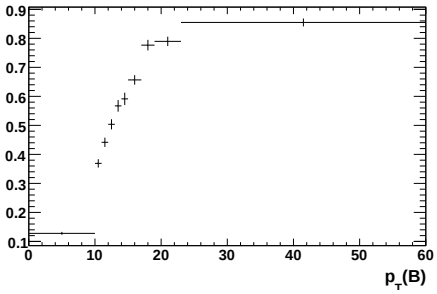

Figure 63: Kaon acceptance

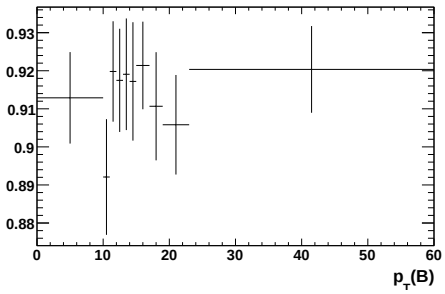

Figure 64: Kaon efficiency

for kaons coming from a B-meson (see fig. 63). Notice that only kaons from a B-meson whose muons lie in the muon acceptance region and whose dimuon mass $m(\mu^+\mu^-)$ is in the $3.0 - 3.2\,\text{GeV}$ window are used for this plot in order to avoid double-counting. From this figure one can see that the probability of reconstructing such a kaon is quite low for low $p_T(B)$ values, but rises up to nearly 90 % for higher p_T (B).

4.3.5 Kaon Reconstruction Efficiency

It is not sufficient for a kaon to lie within the acceptance region to be used for the reconstruction of a B-candidate, similar as for the muon case, there is a certain probability of reconstructing a generated kaon as a kaon, or misidentify it as something else. This probability can be calculated as the ratio of "reconstructed kaons in the acceptance region that are really kaons" and "all generated kaons in the acceptance region". As one can see in figure 64, the reconstruction efficiency of kaons is between 89 % and 92 %, i.e. approximately constant throughout the whole region.

4.3.6 ΔR(J/ψ K) Cut

After a B-meson has been produced, it decays into a J/ψ and K and the J/ψ itself into a muon pair (see fig. 9 in section 3.1). The muons and the kaon then fly nearly in the same direction, because of the boost that the B-meson had before it decayed. For this reason only kaon-candidates within a small angular separation around the J/ψ momentum vector are accepted in the analysis. On this way some of the right candidates could be lost due to this cut. This efficiency thus can be calculated as the number of candidates within the $\Delta R(J/\psi\,, K) < 1.2$ range, divided by the number of candidates before this cut is applied. However taking a look at figure 65 one can recognize that the efficiency value does not fall under the 100 % value for the whole p_T range, i.e. no true candidates are lost. The explanation for this 100 % efficiency lies in figure 20 on page 13, where ΔR-distributions for the signal and the background are shown. All of the signal values lie between the values 0 and 1.2 and thus can not be cut with the restriction of ΔR to be smaller than 1.2.

4.3.7 B Efficiency

In the next step the mass cut is applied on the candidates. Only B-candidates with a mass between 5.0 GeV and 5.5 GeV are accepted for the analysis. The efficiency is then equal to the ratio of the number of candidates passing through the cut and candidates before the cut. In figure 66 this efficiency is plotted against $p_T(B)$ and is nearly 100 % in all p_T-values, meaning that only few false candidates does not fulfill the required mass cut and thus are sorted out.

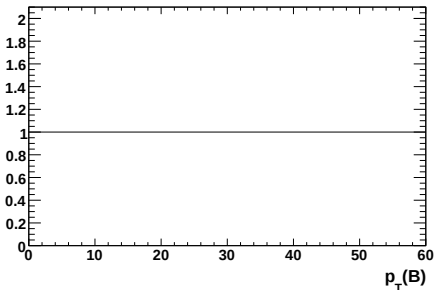

Figure 65: Δ R(J/ψ, K) efficiency

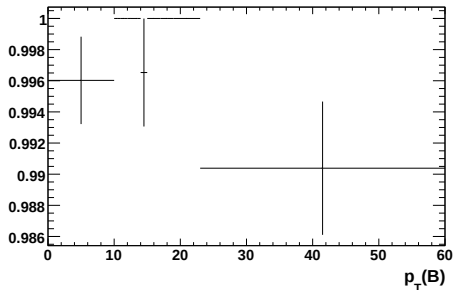

Figure 66: B efficiency

4.3.8 χ^2 Efficiency

The last possibility to get rid of some false candidates was to apply the χ^2 cut (see section 3.3). The efficiency is set to the ratio of "number of candidates before the cut" and "number of candidates after the cut", and is shown in figure 67. The values are quite constant throughout the whole p_T-region and are approximately 99 %. That means that out of 100 B-candidates passing through the χ^2 cut, on average one true candidate is sorted out.

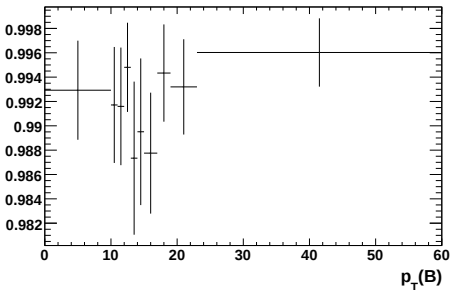

Figure 67: χ^2 efficiency

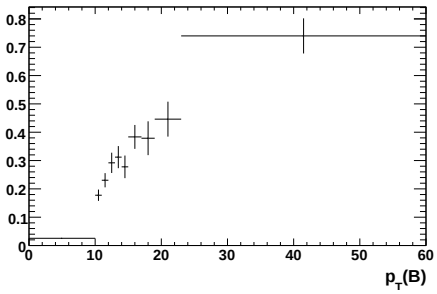

Figure 68: Dimuon efficiency

4.3.9 Dimuon Efficiency

There is one more reduction factor that has to be included in the corrections. In contrary to the other efficiencies, this factor does not come from the analysis, but from the production settings of the signal file. During the production of the signal sample (see section 2.3) a dimuon filter, requiring $p_T(\mu) > 2.5$, $|\eta(\mu)| < 2.5$ and $3.05\,\text{GeV} < m(\mu^+\mu^-) < 3.15\,\text{GeV}$, was used in order to have more $B \to J/\psi(\to \mu^+\mu^-)K$ decays in this sample. In order to find out the number of events that would appear without this filter, one has to compare bin by bin the number of decays produced with a dimuon filter and the number of decays produced without this filter. For this purpose another sample, having the same properties as the signal sample, but without the dimuon filter, was produced. The comparison of the decay numbers resulted in a new efficiency shown in figure 68.

4.3.10 Verification of the Total Efficiency

Before all of the calculated efficiencies can be used for the determination of the differential cross-section, a verification should be done to examine whether they are right or not. The way to do it is to check, if the total generated number of $B \rightarrow J/\psi(\rightarrow \mu^+\mu^-)K$ decays can be deduced out of the reconstructed number of decays using the efficiencies. The generated and the reconstructed number are connected via the following relation:

$$N(p_T)_{B^{\pm}_{gen.}} = \frac{N(p_T)_{B^{\pm}_{reco.}}}{\epsilon_{tot.}} = \frac{N(p_T)_{B^{\pm}_{reco.}}}{\prod \epsilon_i},$$

where ϵ_i denotes the efficiencies calculated in this chapter. Plotting $B^{\pm}_{gen.}$ and $B^{\pm}_{reco.}/\epsilon_{tot.}$ in the same histogram (see fig. 69) one can easily recognize that both have the same shape. This confirms the expectation and allows to use the efficiencies for the differential cross-section.

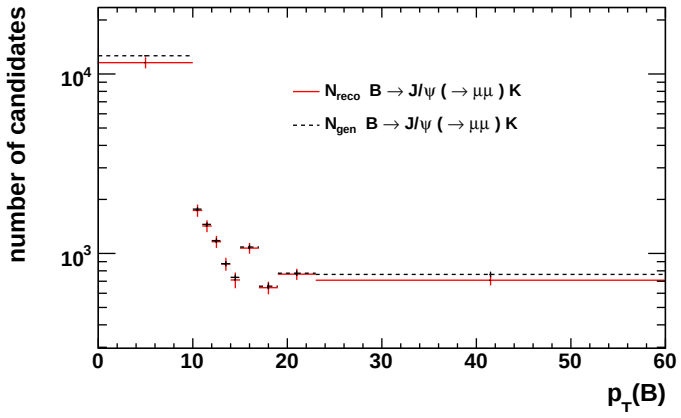

Figure 69: Generated and reconstructed number of $B \rightarrow J/\psi(\rightarrow \mu^+\mu^-)K$ decays

4.4 Cross-Section Results

After all the efficiencies, the number of reconstructed events and the luminosity have been determined, the differential cross-section of the $B^+ \rightarrow J/\psi(\rightarrow \mu^+\mu^-)K^+$ decay can be calculated. Because the goal is the differential and not the total cross-section, all of the contributors have to be read out bin by bin from the according histograms. So for example the number of candidates $N(p_T)_{B^{\pm}_{reco.}}$ in a certain p_T-region can be found out of the histogram 51. The total efficiency $\epsilon_{tot.}$ is calculated bin by bin as the product of all efficiencies of section 4.3. For the width of the bins Δp_T one can take the values from the table 2 in section 4.2. Substituting all these numbers into the formula on page 19, figure 70 can be drawn as the result. Here the differential cross-section computed using the reconstructed number of decays, is compared with the cross-section using generated number of decays for the same sample. The shapes of both distributions are the same, which means that the differential cross-section can be reconstructed quite precisely.

In order to prove the validity of the analysis, the reconstructed differential cross-section was also compared with a generated cross-section of another sample (see fig. 71). This cross-section

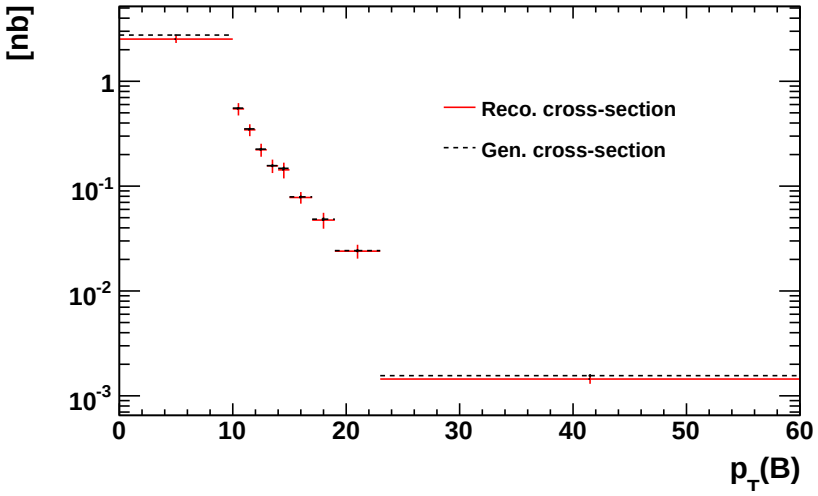

Figure 70: Differential cross-section verification

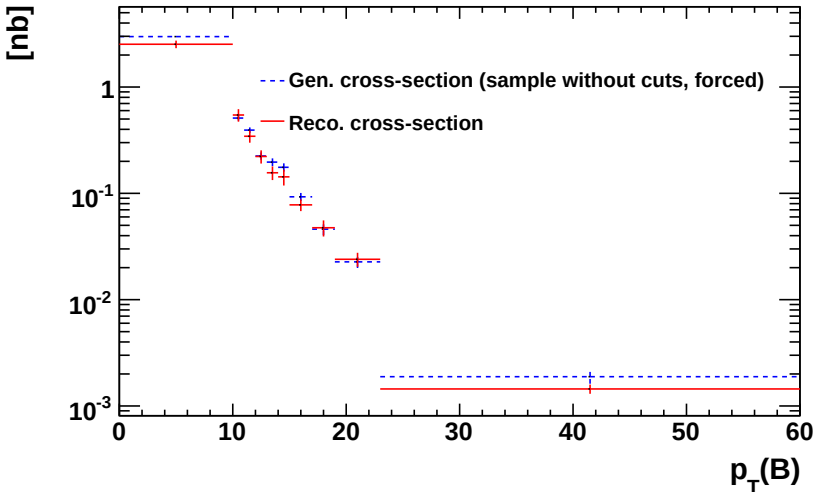

Figure 71: Differential cross-section of $B^+ \to J/\psi\ (\mu^+\mu^-)K^+$ decay

was figured out using an extra sample with no filters at all, by just counting all generated $B^{\pm}$ mesons and then using the cross-section formula without corrections:

$$\frac{d\sigma_{B^+}}{dp_T(B^+)} \times \mathcal{B}(B^+ \to J/\psi K^+) \times \mathcal{B}(J/\psi \to \mu^+\mu^-) = \frac{N(p_T)_{B^{\pm}_{gen.}}}{2 \times \mathcal{L} \times \Delta p_T}.$$

In this sample the $B \to J/\psi(\to \mu^+\mu^-)K$ decay was also forced as in the signal sample, in order to get enough decays for the determination of the cross-section. Also in this figure the shapes of the distributions are very similar. Variations arise due to statistical fluctuations between the two samples.

5 Conclusions

After having found a method for the determination of the differential cross-section of the $B^+ \rightarrow J/\psi(\rightarrow \mu^+\mu^-)K^+$ decay, and having tested it on a sample where this decay was forced, it can now be applied on the unbiased data sample described in section 2.2. The procedure remains the same: to find the differential cross-section, one first has to calculate the luminosity of this sample, find the number of signal events as function of $p_T(B)$ and compute the product of efficiencies, which, on their part, have to be determined first.

5.1 Transverse Momentum Binning

Similar as for the signal sample, the problem of the distribution of the signal events as function of p_T (see fig. 72) has to be treated in a proper way. Also here the number of events decreases toward low and high p_T-values and has a peak between 10 and 11 GeV. Because we are now working on the data sample, there are much less events in this plot and, thus, the binning of the signal sample is unsuitable here. The new p_T-binning is chosen to have only two bins placed as in table 3.

Table 3: New binning

Bin	1	2
Range / GeV	0-13	13-60
Bin width / GeV	13	47

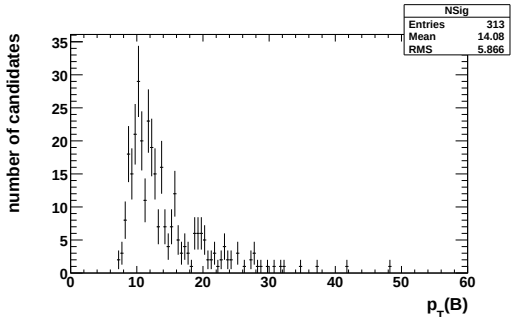

Figure 72: Number of candidates as function of $p_T(B)$

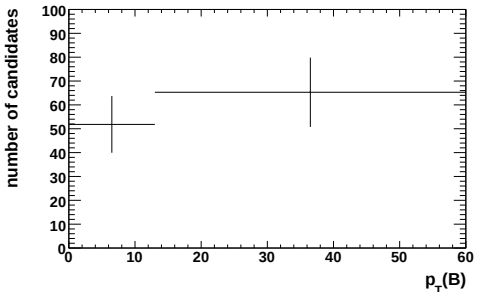

Figure 73: $N_{sig}(p_T)$ with new binning

5.2 Fitting the Peaks

After having set the new binning, one can now fill the masses of the candidates in additional histograms covering each a p_T region of table 3. This time there are only two histograms (see fig. 74). Comparing these figures with histograms on figure 52, one should realize that now there is a linear background and thus, the combined function of section 3.4 is more important for the determination of the number of events in the peak as in the signal sample. After the fit, the numbers of events inside these peaks have been filled in the new histogram (see fig. 73).

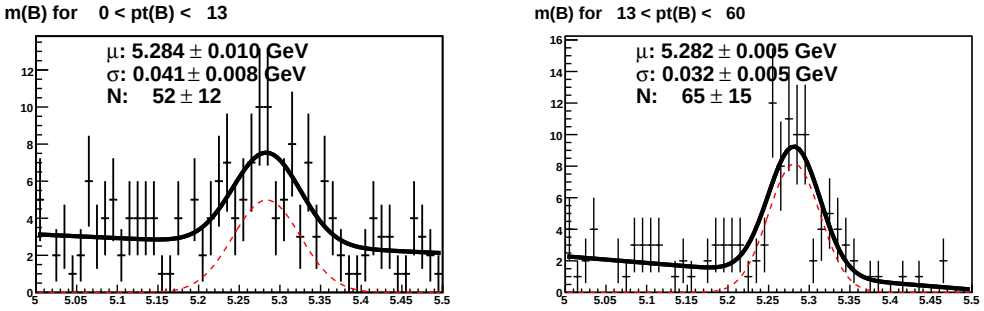

Figure 74: Mass distribution of candidates within different p_T-windows

5.3 Efficiencies and Differential Cross-Section

The next step is to determine the efficiencies needed to correct the number of signal events that has been reduced during the cuts. The efficiencies explained in section 4.3 are redrawn with a new binning in figures 75–83. Substituting all of the numbers bin by bin in the formula for the differential cross-section, figures 84 and 85 can be drawn as the result.

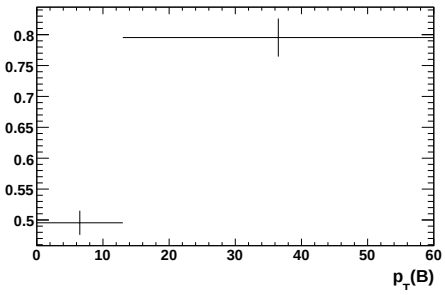

Figure 75: Muon Acceptance

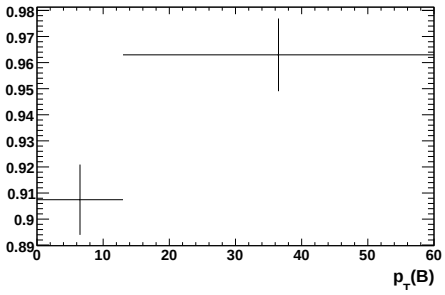

Figure 76: Muon Identification Efficiency

Even for a data sample with an integrated luminosity of only $708\,\mathrm{nb}^{-1}$, the differential cross-section of the $B^+ \to J/\psi\ (\mu^+\mu^-)K^+$ decay can be determined with a very good consistency with the cross-section computed with the number of generated B-mesons of the same sample. Also the comparison with an extra sample produced without cuts is quite satisfiable and, thus, the goal of the thesis is achieved.

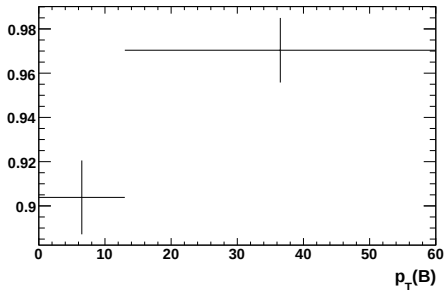

Figure 77: J/ψ Efficiency

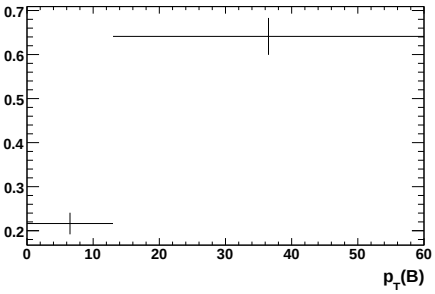

Figure 78: Kaon Acceptance

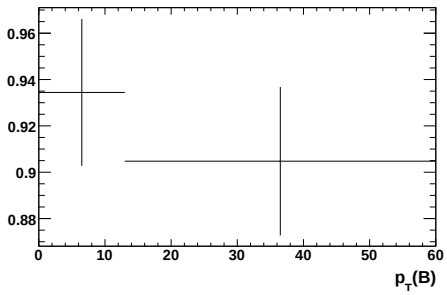

Figure 79: Kaon Efficiency

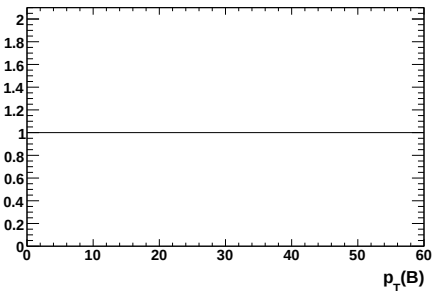

Figure 80: ΔR(J/ψ, K) Efficiency

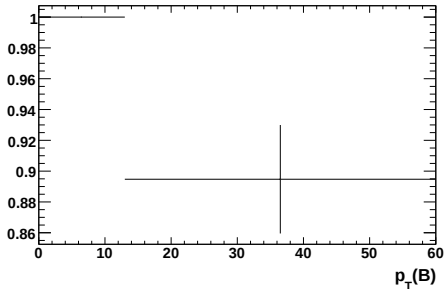

Figure 81: B Efficiency

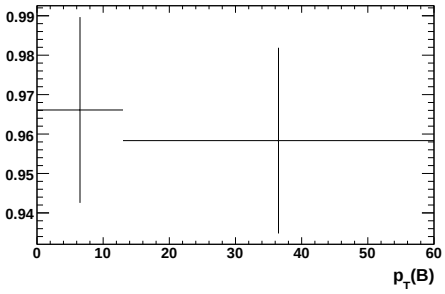

Figure 82: χ^2 efficiency

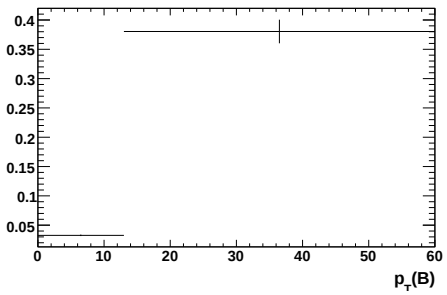

Figure 83: Dimuon efficiency

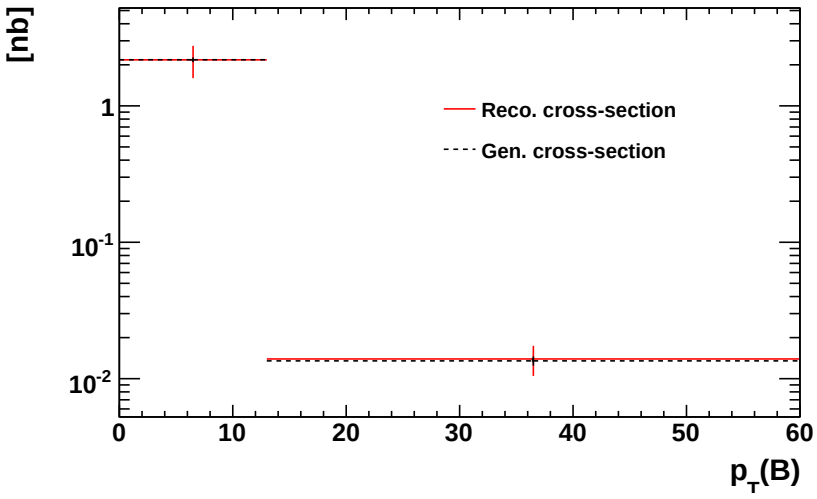

Figure 84: Differential cross-section verification

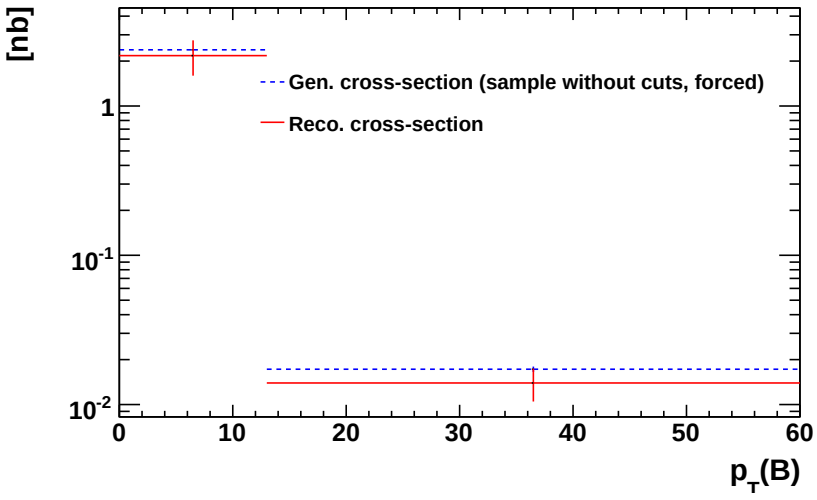

Figure 85: Differential cross-section of $B^+ \to J/\psi(\mu^+\mu^-)K^+$ decay

A Acknowledgments

I would like to express my deep gratitude toward Urs Langenegger for his support, helpful advices and many hours of his precious time he invested in discussions with me. I also want to thank Sarah Dambach and Michael Stueckelberger for a pleasant working environment and useful hints, that helped me creating this thesis. And last but not least I wish to thank Raphael Aardoom and my family, whose moral support encouraged me to invest all my energy in this work.

References

[1] E. Norrbin and T. Sjostrand. Production and hadronization of heavy quarks. *Eur. Phys. J.*, C17:137–161, 2000.

[2] W. M. Yao et al. Review of particle physics. *J. Phys.*, G33:1–1232, 2006.

[3] Michel Della Negra et al. CMS Physics TDR: Volume I (PTDR1), Detector Performace and Software. *CERN-LHCC*, 2006-001, 2006.

[4] Torbjorn Sjostrand, Stephen Mrenna, and Peter Skands. PYTHIA 6.4 physics and manual. *JHEP*, 05:026, 2006.

[5] D. J. Lange. The EvtGen particle decay simulation package. *Nucl. Instrum. Meth.*, A462:152–155, 2001.